

Small-signal Stability Studies of 270V DC Power System for More Electric Aircraft Employing Switched Reluctance Generator Technology

Liqu Han, Jiabin Wang and David Howe

Department of Electronic and Electrical Engineering, University of Sheffield, Mappin Street, Sheffield, S1 3JD, U.K.

Keywords: *Small-signal stability, more-electric aircraft, switched reluctance generator*

Abstract

The paper investigates the small-signal stability of a 270V DC power system for a more electric aircraft, which employs switched reluctance generator technology and multiple distributed power electronic converters for flight control surface actuation, environmental control, and numerous DC and AC loads. Non-linear state space models for the complete system have been established and the eigenvalue method is applied to access the small-signal stability. Time-domain simulations are used to validate the simplified mathematical models and the findings of the proposed analysis technique.

1 Introduction

Currently, aircraft loads are supplied from a combination of individually optimized hydraulic, electrical, pneumatic, and mechanical power sources. However, the use of electrical power alone will enable global optimization and significant system level performance improvements [1]. This is the more-electric aircraft (MEA) concept, and although preferred architectures for MEA power systems have yet to be established, they will feature multiple distributed power electronic converters for flight control surface actuation, environmental control, and numerous DC and AC loads [2]. Further, a MEA power system would include variable speed embedded power generation, which is likely to favor switched reluctance (SR) machine technology because of its high power density, its ability to operate in harsh environments and the fact that it offers a degree of fault-tolerance [3]. However, the

performance of such a power system is problematic due to the fact that power electronic converters generally exhibit constant power characteristics by virtue of their nearly ideal regulation capability, and are, therefore, behave as negative impedance loads. The interaction of these negative impedance loads with the SR generator and its control system may cause instability problems [4][5].

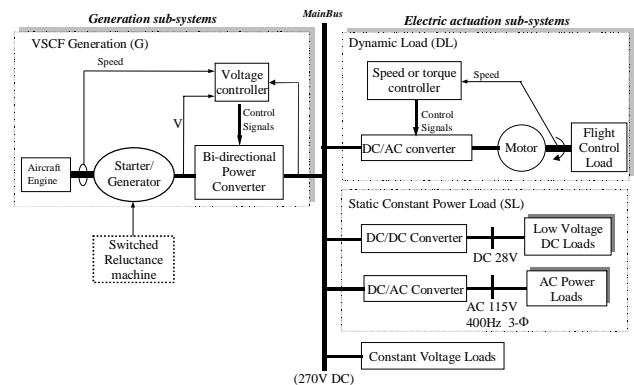


Fig. 1 270V DC power system

This paper assesses the small-signal stability of a simple, yet representative, 270V DC power system, which employs a switched reluctance generator, as shown in Fig. 1. All electric drive sub-systems for flight control surface actuation, such as electro-mechanical actuators (EMA) and electro-hydraulic actuators (EHA) which operate frequently in transient modes, are classified as dynamic loads. The DC/DC and DC/AC converters, which supply various 28V DC loads or 115V/400Hz AC loads for avionics, and other instruments and electronic equipment, are considered as static loads. Both static and dynamic loads are controlled by power electronic converters and therefore

exhibit constant power characteristics. The system also includes passive loads, referred to as constant voltage loads, for cabin service equipment and electrical lighting systems etc.

2 Modeling of the Power System Architecture

2.1 Drive Sub-system

Without loss of generality, a dynamic load for flight control surface actuation is represented by a three-phase inverter-fed drive sub-system, as shown in Fig. 2. The drive controller usually consists of an inner current/torque control loop and an outer speed/position control loop, as shown in Fig.3 (a). The function $f(u)$ represents the mapping between the torque demand and the motor current demand and is dependent on a particular drive technology being employed. The current control loop regulates the motor current via pulse width modulation (PWM) and provides appropriate electronic commutation signals for the inverter operation. Since the mechanical time constant is usually much greater than the electrical time constant. The inner loop may be simplified to a first-order delay with the desired current loop time constant T_m , as shown in Fig.3 (b).

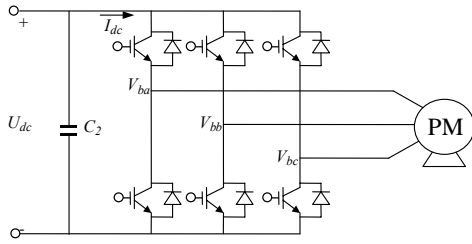


Fig. 2. Schematic of an inverter fed drive sub-system

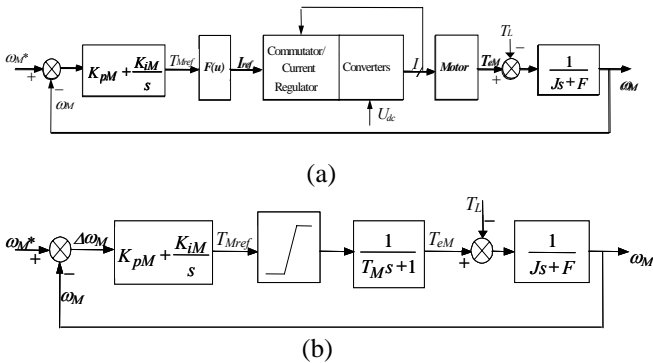


Fig. 3 Drive sub-system model

The state-space equations for the drive sub-system operating in the linear control region are given by:

$$\begin{cases} \frac{d\omega_M}{dt} = -\frac{F}{J}\omega_M + \frac{1}{J}T_{eM} - \frac{1}{J}T_L \\ \frac{dT_{eM}}{dt} = -\frac{K_{pM}}{T_m}\omega_M - \frac{1}{T_m}T_{eM} + \frac{1}{T_m}x_M + \frac{K_{pM}}{T_m}\omega_M^* \\ \frac{dx_M}{dt} = -K_{iM}\omega_M + K_{iM}\omega_M^* \end{cases} \quad (1)$$

where ω_M , and T_{eM} are the motor output speed and torque, T_L is the load torque, F and J is the viscous friction coefficient and moment of inertia of the drive system, and K_{pM} , and K_{iM} is the proportional and integral control gains of the speed loop. x_M represents the internal state of the PI speed controller.

However, this tightly regulated drive sub-system indeed behaves as a constant power load to the DC supply network, which can be illustrated as follows. In steady state, the output power of the inverter is given by:

$$P_{out} = 3V_m I_m \cos \varphi \quad (2)$$

where V_m , I_m and $\cos \varphi$ are the rms motor voltage, current, and power factor at a specific operating point. If the inverter loss is negligible, the inverter input power should be equal to its output power, i.e.

$$\begin{aligned} U_{dc} I_{dc} &= 3V_m I_m \cos \varphi \quad \text{or} \\ I_{dc} &= 3 \frac{V_m}{U_{dc}} I_m \cos \varphi = 3m I_m \cos \varphi \end{aligned} \quad (3)$$

where I_{dc} is the average inverter DC link current over a switching period and U_{dc} is the DC supply voltage. $m = \frac{V_m}{U_{dc}}$ is defined as a

generalised modulation index. In a state-of-the-art digitally controlled drive, the amplitude $\sqrt{2}V_m$ of the motor input voltage (demand) is the output of the current control loop and is realized by inverter PWM operation via adjusting the modulation index m against measured DC link voltage U_{dc} in each sampling

period. If the supply voltage U_{dc} varies from U_{dc1} to U_{dc2} due to a disturbance in the network, the current controller output voltage $\sqrt{2}V_m$ has to be maintained constant in order to achieve the same output speed and torque (or the same output power). Consequently the modulation index will be adjusted by the digital PWM modulator to vary from $m_1 = V_m / U_{dc1}$ to $m_2 = V_m / U_{dc2}$. It follows from (3) that over one switching cycle, I_{dc} will varies from $i_{dc1} = \frac{3V_m I_m \cos \varphi}{U_{dc1}}$ to $i_{dc2} = \frac{3V_m I_m \cos \varphi}{U_{dc2}}$, i.e. from $I_{dc1} = P_{out} / U_{dc1}$ to $I_{dc2} = P_{out} / U_{dc2}$. Thus I_{dc} increases as U_{dc} decreased in one switching cycle or vice versa, and the drive subsystem behaves like a negative impedance load to the power system.

2.2 SR Generator Sub-system

Fig. 4 shows the schematic of the switched reluctance generator (SRG) sub-system. The SR generator is usually connected to the DC bus via asymmetric H-bridges. Torque in the SR machine is produced by the natural tendency of the stator poles to attract the nearest rotor poles. If the phase is excited as the rotor poles rotate through the aligned position when the phase inductance decreases with the rotor position θ , ($dL/d\theta < 0$) as illustrated in Fig. 5 (a), the rotor experiences torque opposing to its direction of rotation and hence the machine operates as a generator. The generator speed varies with the engine speed over a speed range of 1 to 2 times the base speed. Below the base speed, the output power can be controlled by regulating the phase current with fixed turn-on and turn-off angles, Fig. 5 (b) [6]. When operating above the base speed, the SR generator enters the single pulse operation mode and the output power is controlled by variation of the turn-on and turn-off angles, Fig. 5 (c) [7].

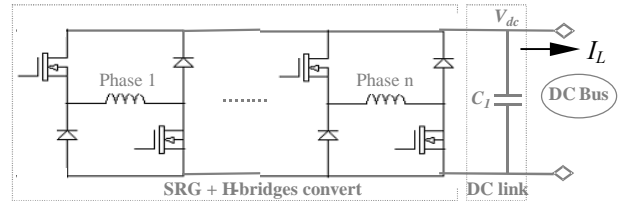


Fig. 4 SR generator sub-system

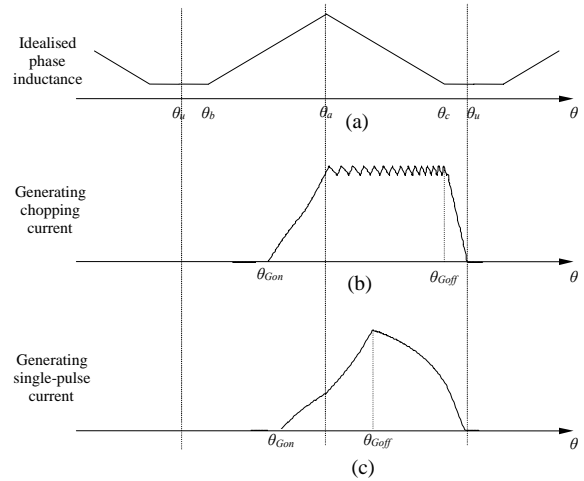


Fig. 5 Idealized SR machine inductance variation (a) and SR generator control modes: current control mode (b) and single pulse control mode (c)

The output power of the SR generator is usually regulated by a voltage controller, which is typically a proportional-integral (PI) controller, so that the bus voltage is maintained close to its nominal value of $V_{dc}^* = 270V$. An inner current/torque control loop is also employed, as shown in Fig. 6 (a), to improve the power control response and to reduce the effect of back-emfs on the voltage control loop. Torque control is achieved by regulating the current via pulse-width modulation (PWM) when operating below the base speed, or by varying the turn-on and turn-off angles above the base speed.

Since the torque/current control loop response is much faster than that of the voltage loop, the relationship between the power/torque output and demand may be represented by a first-order delay with a time constant T_g when the torque/current PI controller operates in its linear region. Therefore, the generation sub-system model can be simplified to that shown in Fig. 6(b).

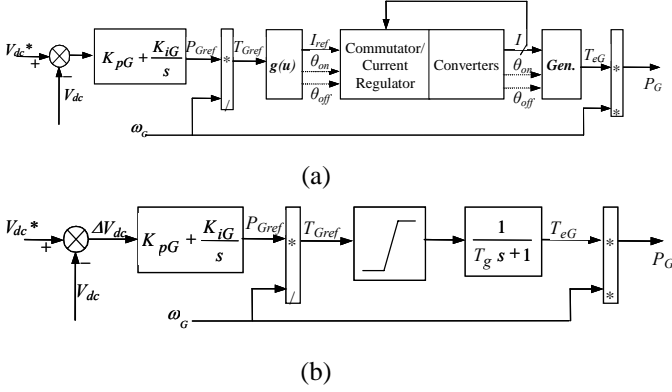


Fig. 6 SR Generator sub-system model

The voltage controller gains, K_{pG} and K_{iG} , may be determined by assuming an ideal current loop response with no delay. The DC bus voltage, V_{dc} , is related to the nominal demand voltage, V_{dc}^* , and the load power P_L by the following equation:

$$V_{dc} = \frac{\frac{K_{pG}}{C_1 V_{dc}^*} s + \frac{K_{iG}}{C_1 V_{dc}^*}}{s^2 + \frac{K_{pG}}{C_1 V_{dc}^*} s + \frac{K_{iG}}{C_1 V_{dc}^*}} V_{dc}^* + \frac{1}{C_1 V_{dc}^*} \frac{s}{s^2 + \frac{K_{pG}}{C_1 V_{dc}^*} s + \frac{K_{iG}}{C_1 V_{dc}^*}} P_L \quad (4)$$

Thus, if the desired voltage control loop bandwidth (or natural frequency) and damping ratio are given by ω_{nG} and ζ_G , respectively, the gains, K_{pG} and K_{iG} can be obtained from:

$$\begin{cases} K_{pG} = 2\zeta_G \omega_{nG} C_1 V_{dc}^* \\ K_{iG} = \omega_{nG}^2 C_1 V_{dc}^* \\ V_{dc}^* = 270 \end{cases} \quad (5)$$

The state-space equation for the generator sub-system when operating at a constant speed is, therefore, given by:

$$\begin{cases} \frac{dP_G}{dt} = -\frac{1}{T_g} P_G + \frac{1}{T_g} x_G - \frac{K_{pG}}{T_g} V_{dc} + \frac{K_{pG}}{T_g} V_{dc}^* \\ \frac{dx_G}{dt} = -K_{iG} V_{dc} + K_{iG} V_{dc}^* \\ \frac{dV_{dc}}{dt} = \frac{P_G}{C_1 V_{dc}} - \frac{1}{C_1} I_L \end{cases} \quad (6)$$

where P_G is the generator output power, C_1 is the DC bus filter capacitor, I_L is the output current of the SR generator sub-system and x_G is the internal state of the voltage PI controller.

2.3 Simplified DC Power System Model

The SR generator sub-system and the drive sub-system are connected to the DC power system via an R - L - C network which represents the effects of the transmission line (R , L) and the load filter (C_2), as shown in Fig. 7. The drive sub-system is represented by a dynamic load DL. A static constant-power load SL (such as a DC-AC converter supplying avionics systems) and a constant-voltage load R_L (such as cabin services electrical loads) are also represented in the model. Both the static and dynamic loads are controlled by power electronic converters which draw constant power at their inputs. Consequently, they behave like negative impedance loads to the power system.

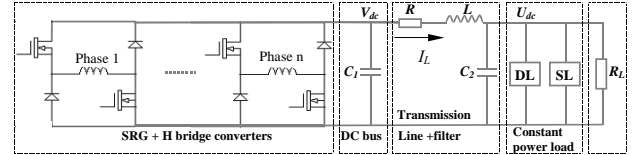


Fig. 7 Simplified 270V DC power system model with SR generator

2.4 State-space equations

When the SR generator and drive subsystems operate in the linear control region, and assuming that the power drawn from the DC supply by the drive-subsystem can be approximated by its output power ($T_{eM}\omega_M$), the state-space equations which govern the dynamic behavior of the system in Fig. 7 can be derived by combining the drive-subsystem state-space equations (1) and the generator sub-system state space equations (6) with the circuit equations governing the RLC network, and are given in equations (7), where U_{dc} is the load side DC bus voltage and P_s is the total power drawn by static constant power loads. R and L are the cable resistance and inductance, respectively.

$$\begin{cases}
 \frac{d\omega_M}{dt} = -\frac{F}{J}\omega_M + \frac{1}{J}T_{eM} - \frac{1}{J}T_L \\
 \frac{dT_{eM}}{dt} = -\frac{K_{pM}}{T_m}\omega_M - \frac{1}{T_m}T_{eM} + \frac{1}{T_m}x_M + \frac{K_{pM}}{T_m}\omega_M^* \\
 \frac{dx_M}{dt} = -K_{iM}\omega_M + K_{iM}\omega_M^* \\
 \frac{dP_G}{dt} = -\frac{1}{T_g}P_G + \frac{1}{T_g}x_G - \frac{K_{pG}}{T_g}V_{dc} + \frac{K_{pG}}{T_g}V_{dc}^* \\
 \frac{dx_G}{dt} = -K_{iG}V_{dc} + K_{iG}V_{dc}^* \\
 \frac{dV_{dc}}{dt} = \frac{P_G}{C_1V_{dc}} - \frac{1}{C_1}I_L \\
 \frac{dI_L}{dt} = -\frac{R}{L}I_L + \frac{V_{dc}}{L} - \frac{U_{dc}}{L} \\
 \frac{dU_{dc}}{dt} = \frac{1}{C_2}I_L - \frac{T_{eM}\omega_M + P_s}{C_2U_{dc}} - \frac{1}{C_2R_L}U_{dc}
 \end{cases} \quad (7)$$

3 Small-signal Stability Studies

The small-signal stability of the system represented by equations (7) has been studied by evaluating the eigenvalues of its Jacobian matrices, which are given in equations (8). As will be seen, the Jacobian matrix is dependent on the drive control parameters (K_{pM} , K_{iM} and T_m), the filter parameters (C_1 and C_2), the cable resistance R and inductance L , the operational conditions (ω_{M0} , T_{eM0} , V_{dc0} , P_s and R_L), and the generator subsystem control parameters (K_{pG} , K_{iG} and T_g).

$$\mathbf{A} = \begin{bmatrix}
 -\frac{F}{J} & \frac{1}{J} & 0 & 0 & 0 & 0 & 0 & 0 & 0 \\
 \frac{K_{pM}}{T_m} & -\frac{1}{T_m} & \frac{1}{T_m} & 0 & 0 & 0 & 0 & 0 & 0 \\
 -K_{iM} & 0 & 0 & 0 & 0 & 0 & 0 & 0 & 0 \\
 0 & 0 & 0 & -\frac{1}{T_g} & \frac{1}{T_g} & -\frac{K_{pG}}{T_g} & 0 & 0 & 0 \\
 0 & 0 & 0 & 0 & 0 & -K_{iG} & 0 & 0 & 0 \\
 0 & 0 & 0 & \frac{1}{C_1V_{dc0}} & 0 & -\frac{P_{G0}}{C_1(V_{dc0})^2} & -\frac{1}{C_1} & 0 & 0 \\
 0 & 0 & 0 & 0 & 0 & \frac{1}{L} & -\frac{R}{L} & -\frac{1}{L} & 0 \\
 -\frac{T_{eM0}}{C_2U_{dc0}} & -\frac{\omega_{M0}}{C_2U_{dc0}} & 0 & 0 & 0 & 0 & \frac{1}{C_2} & \frac{(T_{eM0}\omega_{M0} + P_s)}{C_2(U_{dc0})^2} & -\frac{1}{C_2R_L}
 \end{bmatrix} \quad (8)$$

Further, the sensitivity of the i^{th} eigenvalue λ_i to the element a_{kj} of the Jacobian matrix can be evaluated by the product of the j^{th} element, ϕ_{ji} , of the i^{th} right eigenvector and the k^{th} element, ψ_{ki} , of the i^{th} left eigenvector [8]:

$$\frac{\partial \lambda_i}{\partial a_{kj}} = \phi_{ji} \psi_{ki} \quad (9)$$

The sensitivity of the i^{th} eigenvalue λ_i to the k^{th} diagonal element a_{kk} of the Jacobian matrix, given by equation (10), is known as the

participation factor and is indicative of relative strength of the interaction between the i^{th} system mode, and the k^{th} state state variable.

$$p_{ki} = \frac{\partial \lambda_i}{\partial a_{kk}} = \phi_{ki} \psi_{ik} \quad (10)$$

Table 2 shows the participation factor of the power system at a given operating point. As will be seen, the three drive sub-system state variables and their associated eigenvalues (λ_1 , λ_2 , λ_3) are decoupled from the rest of the system in small signal sense. Further by analyzing the sensitivity of these three eigenvalues, it can be shown that they are only dependent on the operating condition (ω_{M0} , T_{eM0}) and control parameters (K_{pM} , K_{iM} , and T_m) of the drive sub-system. Conversely, the other five eigenvalues are independent of the drive sub-system control parameters but are influenced by the total power of the drive sub-system, the control parameters (K_{pG} , K_{iG} and T_g) of the generator sub-system, the filter capacitances, the cable parameters as well as operating conditions (V_{dc0} , P_s and R_L). Fig. 8 shows the eigenvalue sensitivity to these parameters and operating conditions.

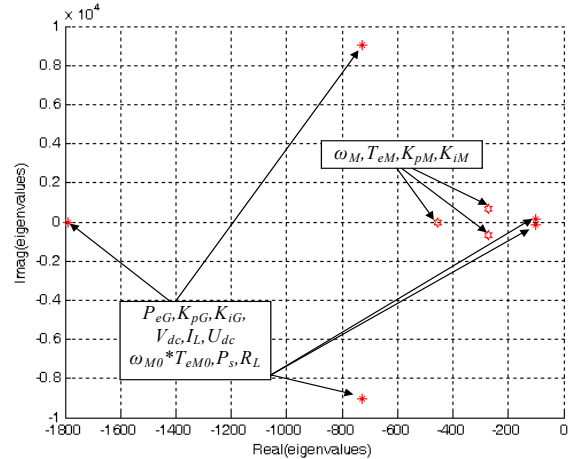


Fig. 8 Eigenvalue sensitivity map

Since the drive sub-system is effectively decoupled from the complete system in small signal sense, the study of the small signal stability of the DC power network can be performed by replacing the drive sub-system as a constant power load. Consequently, state-space equation can be further simplified in (11) where P_{CPL} denotes the total power of all constant power loads connected to the system.

$$\begin{cases}
 \frac{dP_G}{dt} = -\frac{1}{T_g}P_G + \frac{1}{T_g}x_G - \frac{K_{pG}}{T_g}V_{dc} + \frac{K_{pG}}{T_g}V_{dc}^* \\
 \frac{dx_G}{dt} = -K_{iG}V_{dc} + K_{iG}V_{dc}^* \\
 \frac{dV_{dc}}{dt} = \frac{P_G}{C_1V_{dc}} - \frac{I_L}{C_1} \\
 \frac{dI_L}{dt} = -\frac{RI_L}{L} + \frac{V_{dc}}{L} - \frac{U_{dc}}{L} \\
 \frac{dU_{dc}}{dt} = \frac{I_L}{C_2} - \frac{P_{CPL}}{U_{dc}} - \frac{U_{dc}}{R_L}
 \end{cases} \quad (11)$$

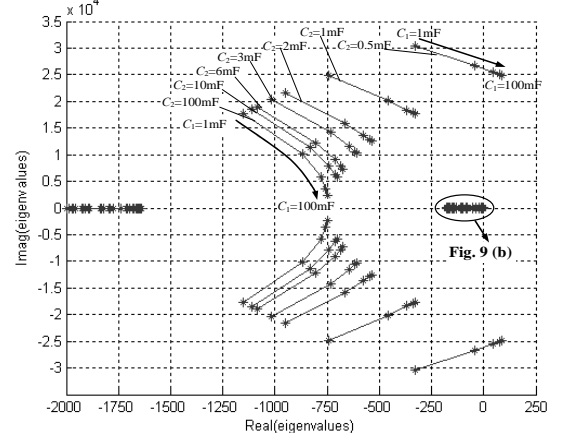
Fig. 9(a) shows the influence of the filter capacitors C_1 and C_2 on the loci of the five eigenvalues when the SR generator supplies an output power of 60kW to purely constant-power loads via a 15m cable whose parameters are given in Table 1. The DC bus voltage is 270V and the voltage control bandwidth is set to 51 Hz (320 rad/s). As will be seen, since the real eigenvalue in the left-half s-plane is far away from the imaginary axis, the system stability is essentially dominated by the two conjugate pairs, one of which has a much higher natural frequency. Fig. 9 (b) shows the zoomed view of the loci of the pair of eigenvalues with low natural frequency. It is evident that C_2 has a significant influence on the eigenvalues of the high frequency pair, and less influence on the low frequency pair, especially when C_1 is large. Further, a small value of C_2 results in less damping on the eigenvalues of the high frequency pair and, hence, more oscillatory response, and may even lead to instability when C_1 is large. Thus, in order to avoid the eigenvalues of the high frequency pair being dominant, C_2 must be sufficiently large. Fig. 9(c) shows the influence of the two capacitances on the damping ratios of the eigenvalues of the low frequency pair. From these figures, appropriate values for C_1 and C_2 can be chosen.

Resistance (ohms/m)	Inductance (uH/m)
0.00016	0.108

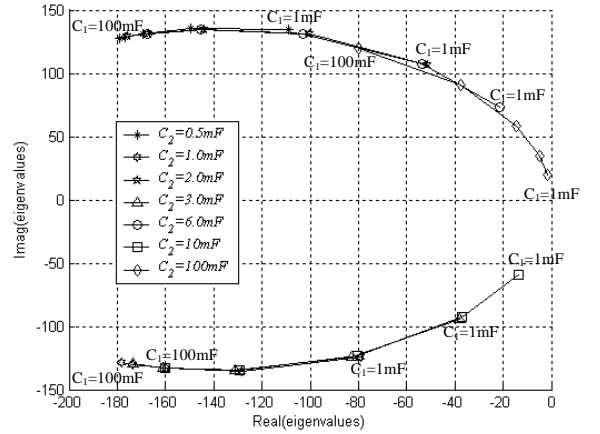
Table 1 Cable parameters of transmission line

Fig. 10 shows the variation of the dominant-pair eigenvalues with the voltage controller bandwidth and the delay time of the inner torque/current (power) control loop. It can be seen that when the delay time, T_g , is relatively large, an increase in the voltage control

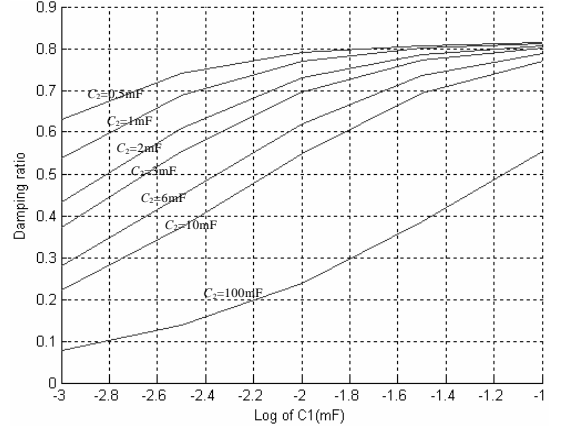
bandwidth will result in the dominant-pair eigenvalues moving to the right-half s-plane, and the system becomes unstable. Hence, an appropriate voltage control bandwidth should be chosen based on a realistically achievable current (power) loop response time in order to maximize the system stability margin.



(a) Loci of five eigenvalues



(b) Loci of low frequency pair eigenvalues



(c) Damping ratio of low frequency pair eigenvalues

Fig. 9 Influence of DC bus and load filter capacitances on eigenvalues

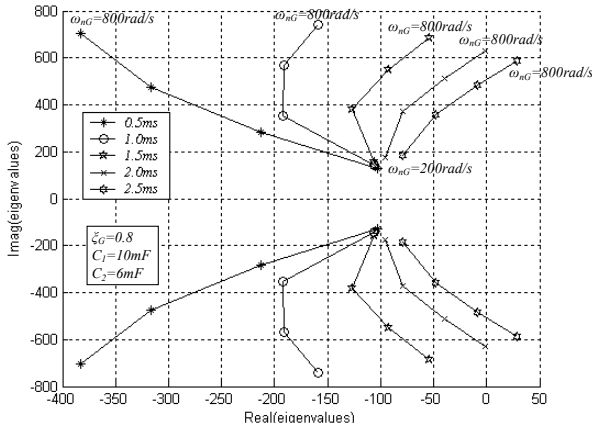


Fig. 10 Influence of voltage and current control bandwidth on eigenvalues

4 Time-domain simulations

Time-domain simulations using detailed power system models to represent the behavior of the SR generator, the drive sub-system for dynamic loads, the static constant power load, the passive components, the power electronic converters /inverters, and various control functions established in the Matlab/Simulink environment in conjunction with the SimPowerSystem™ Toolbox, have been undertaken to support the findings of the state space model established in section 2 and analyzed in section 3.

Fig. 11 shows the transient responses of the load side DC bus voltage, the average current and power over one PWM cycle drawn by the drive sub-system inverter when a constant voltage load ($R_L = 5\text{ohm}$) is switched on at $t = 0.02$ (s). The permanent magnet motor drive sub-system operates at 1500rpm with 200Nm load torque, and is controlled by an inner current loop and an outer speed loop. The space vector modulation technique is used to generate the switching signals for the inverter, and the modulation index is adjusted according to the output voltage demand of the current control loop and the measured DC bus voltage. As will be seen, a step demand of the passive load results in a DC bus voltage dip. However, due to rapid adjustment of the modulation index, the motor operation is not affected in that the total power drawn by the inverter sub-system is maintained

constant, and the inverter input current increase as the bus voltage decreases.

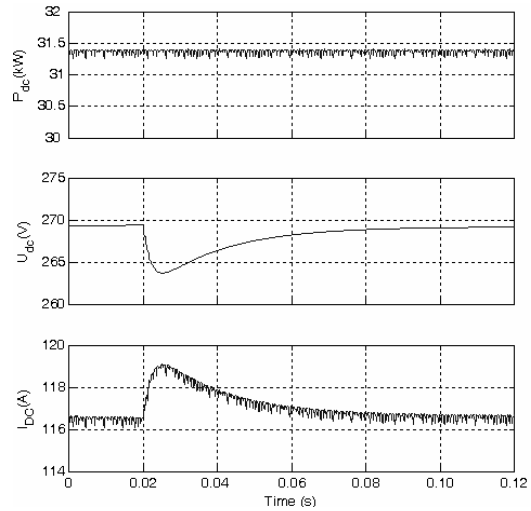


Fig. 11 Transient responses with a drive subsystem

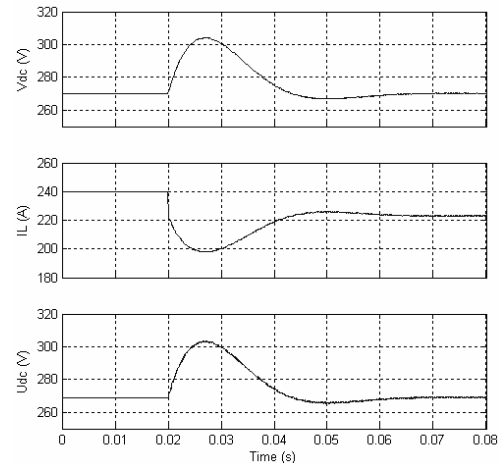


Fig. 12 Transient responses with constant power load when $C_1=1\text{mF}$ and $C_2=0.5\text{mF}$

Fig. 12 shows the transient responses of the DC bus voltage and current, and the load voltage when an initial 65 kW resistive load is suddenly switched to a 60kW constant power load. The values of C_1 and C_2 are 1mF and 0.5 mF, respectively, and the other parameters and conditions being the same as those which were assumed in deriving Fig. 9. As can be seen, the transient responses are stable but exhibit overshoot due to the relatively low damping ratio, as is evident in Fig. 9. However, if C_1 is increased to 100mF, the transient responses become unstable as shown in Fig. 13. This instability is also predicted in Fig. 9. Thus both time-domain simulation results are consistent

with those obtained by the eigenvalue analysis

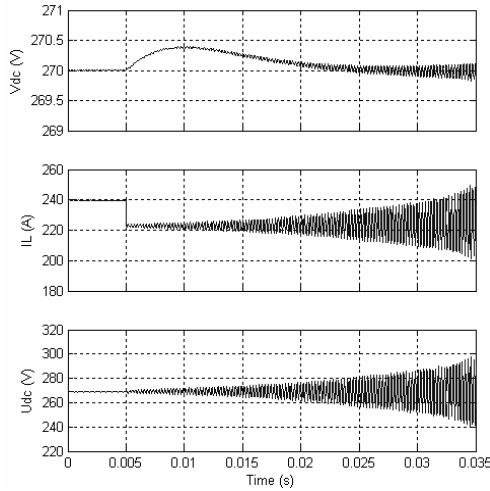


Fig. 13 Transient responses with constant power load when $C_1=100\text{mF}$ and $C_2=0.5\text{mF}$

5 Conclusions

Non-linear state-space models representing the dynamic behavior of a representative 270V DC MEA power system have been established, the small-signal stability of the system has been assessed by analyzing the eigenvalues and participation factor of the Jacobian matrices. It has been shown that control parameters of the motor drive sub-system have no influence on the small signal stability of the power system. However, the voltage controller gains of the generator sub-system, and the DC bus and load filter capacitances have profound influences on the system stability. Time-domain simulations, using detailed system models established in the

based on the simplified system model. Matlab/Simulink environment, have further supported the results of the eigenvalue analysis.

References

- [1] Quigley R. More electric aircraft. Proc. Of 1993 IEEE Applied Power Electronics Conf, San Diego, pp. 906-911, 1993.
- [2] Emadi A, and Ehsani M. Electrical system architecture for future aircraft. Proc. of 34th Intersociety Energy Conversion Engineering Conf., British Columbia, pp.1-5, 1999.
- [3] Elbuluk M and Kankam M. Potential starter/generator technologies for future aerospace application. IEEE AES System Magazine, pp. 24-31, 1997.
- [4] Emadi A, and Ehsani M. Negative impedance stabilizing controls for PWM DC/DC converters using feedback linearization techniques. Energy Conversion Engineering Conference and Exhibit, 2000 (IECEC), 35th Intersociety, vol. 1, pp. 613-620, 2000.
- [5] Sudhoff S, Glover S, Lamm P, Schmucker D and Delisle D. Admittance space stability analysis of power electronics systems. IEEE Trans. on Aerospace and Electronic Systems, Vol. 36, No. 2, pp. 965-973, 2000.
- [6] Ferreira C, Jones S, Heglund W, and Jones W. Detained design of a 30-kW switched reluctance starter/generator system for a gas turbine engine application. IEEE Tran. On Industry Applications, vol. 31, No. 6, pp. 553-561, 1995.
- [7] Torrey D. Switched reluctance generators and their control. IEEE Tran. On Industry Applications, vol. 49, No. 1, pp.3-14, 2002.
- [8] Kundur P. Power system stability and control, McGraw Hill, USA, 1994.

	λ_1	λ_2	λ_3	λ_4	λ_5	λ_6	λ_7	λ_8
ω_M	0.48637	0.75535	0.75535	0	0	0	0	0
Te_M	0.40231	0.55994	0.55994	0	0	0	0	0
x_M	1.08410	0.34111	0.34111	0	0	0	0	0
P_G	0	0	0	1.11650	0.00146	0.00146	0.06263	0.06263
x_G	0	0	0	0.00975	0.00002	0.00002	0.67406	0.67406
V_{dc}	0	0	0	0.08160	0.19024	0.19024	0.44507	0.44507
I_L	0	0	0	0.00323	0.50031	0.50031	0.00025	0.00025
U_{dc}	0	0	0	0.04789	0.31153	0.31153	0.26978	0.26978

Table 2 Participation factor of the DC power system under the given operational condition ($\omega_{M0}=1500$ rpm, $T_{eM0}=200\text{Nm}$, $V_{dc0}=270\text{V}$, $P_s=0$ and $R_L=0$)